ACS NANO

www.acsnano.org

ARTICLE

Observation of Rich Defect Dynamics in Monolayer MoS_2

Harikrishnan Ravichandran, Theresia Knobloch, Andrew Pannone, Alexander Karl, Bernhard Stampfer, Dominic Waldhoer, Yikai Zheng, Najam U Sakib, Muhtasim Ul Karim Sadaf, Rahul Pendurthi, Riccardo Torsi, Joshua A. Robinson, Tibor Grasser, and Saptarshi Das*

Cite This: *ACS Nano* 2023, 17, 14449–14460

Read Online

ACCESS | Metrics & More | Article Recommendations | Supporting Information

ABSTRACT: **Defects play a pivotal role in limiting the performance and reliability of nanoscale devices. Field-effect transistors (FETs) based on atomically thin two-dimensional (2D) semiconductors such as monolayer MoS_2 are no exception. Probing defect dynamics in 2D FETs is therefore of significant interest. Here, we present a comprehensive insight into various defect dynamics observed in monolayer MoS_2 FETs at varying gate biases and temperatures. The measured source-to-drain currents exhibit random telegraph signals (RTS) owing to the transfer of charges between the semiconducting channel and individual defects. Based on the modeled temperature and gate bias dependence, oxygen vacancies or aluminum interstitials are probable defect candidates. Several types of RTSs are observed including anomalous RTS and giant RTS indicating local current crowding effects and rich defect dynamics in monolayer MoS_2 FETs. This study explores defect dynamics in large area-grown monolayer MoS_2 with ALD-grown Al_2O_3 as the gate dielectric.**

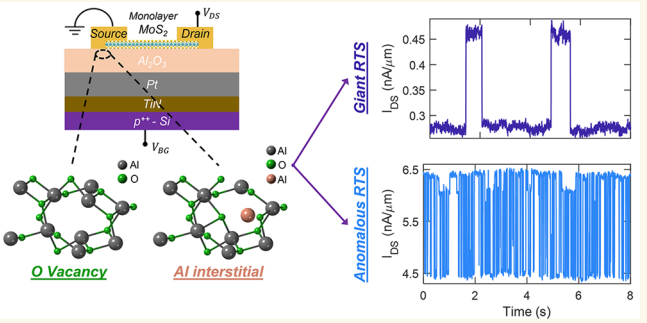

KEYWORDS: *random telegraph signals, MoS_2, Al_2O_3, defects, field-effect transistors, charge trapping, reliability*

According to the International Roadmap for Devices and Systems (IRDS), atomically thin and semiconducting transition metal dichalcogenides (TMDCs) such as monolayer MoS_2 are promising alternatives to silicon for both low-power and high-performance logic devices at advanced technology nodes.[1−3] Recent developments in high-performance field-effect transistors (FETs) based on large-area-synthesized monolayer MoS_2 and demonstration of integrated circuits for digital, analog, radio frequency (RF), and brain-inspired electronics justify its inclusion in the IRDS.[4−16] Unsurprisingly, most studies on MoS_2 FETs focus on improvement in large-area growth,[17] optimization of transfer and fabrication process flow,[14,18,19] contact and mobility engineering,[20−22] the realization of scaled devices,[23,24] etc., to meet the theoretical performance limit predicted by numerical simulations. However, less emphasis is placed on understanding the nature and origin of defects in MoS_2 FETs, which can ultimately limit performance and raise reliability concerns.

Defects in MoS_2 FETs can reside in the semiconducting channel, such as sulfur vacancies, or at the channel/dielectric interface, or in the dielectric stack. Their origin can be ascribed to growth imperfection, film transfer, fabrication processes, and fundamental properties of the gate dielectrics and their distinct defect bands.[25,26] During device operation, these defects can exchange charges with the channel, affecting device performance and reliability.[26,27] Most reliability studies on MoS_2 FETs involve the investigation of bias temperature instabilities (BTIs),[28] which occur due to charge trapping in the oxide[29,30] or at the trapping sites introduced by adsorbates and water molecules at the interface.[31,32] Charge trapping can lead to a decrease in the field-effect mobility, worsening of the subthreshold slope, and hysteresis in the device transfer characteristics as well as permanent or partially recoverable threshold voltage shifts.

Whereas BTI is a useful approach for studying the reliability of 2D FETs, a better understanding of the physical mechanisms of charge trapping and the nature of the involved defects can be obtained via the characterization of individual defects. Such characterization, however, requires ultrascaled devices, which contain only a few defects within the channel

Received: December 30, 2022
Accepted: July 10, 2023
Published: July 25, 2023

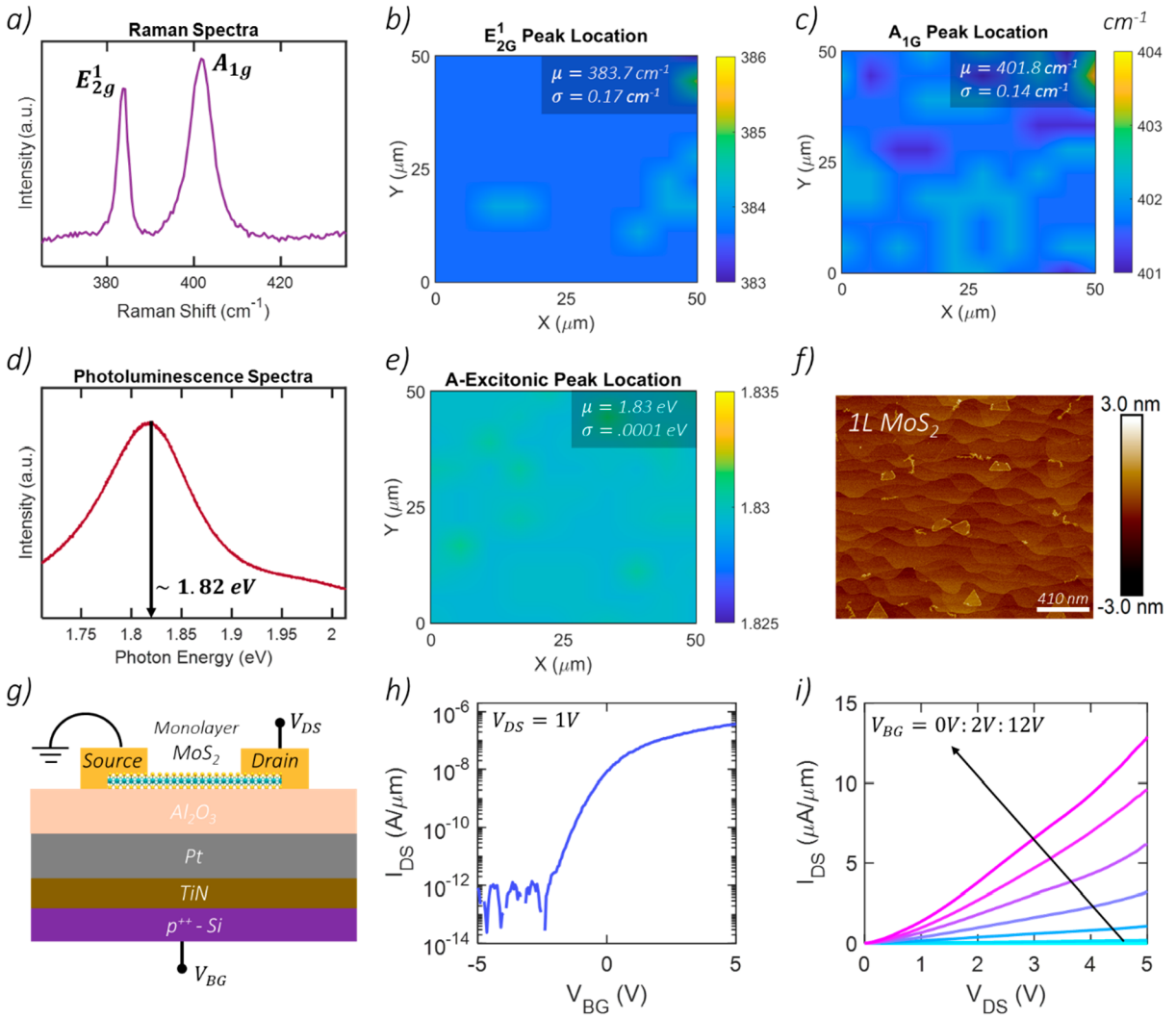

Figure 1. Fabrication and characterization of monolayer MoS_2 field-effect transistor (FET). (a) Raman spectra obtained from the MoS_2 film showing the characteristic in-plane E^1_{2g} and out-of-plane A_{1g} modes at 384 and 402 cm^{-1}, respectively, with a peak-to-peak distance of ~18 cm^{-1}. Raman maps for (b) E^1_{2g} and (c) A_{1g} peak positions measured over a 50 μm × 50 μm area. The mean and standard deviation values are shown in the inset. (d) Photoluminescence (PL) spectra with a characteristic monolayer peak at 1.82 eV. (e) Color map for the PL peak position, measured over a 50 μm × 50 μm area. The mean PL peak position was found to be at ~1.83 eV with a standard deviation of ~0.001 eV. (f) Atomic force microscopy (AFM) micrographs of the MoS_2 film indicating a coalesced monolayer film with a few oriented bilayer domains on top and a thickness of ~0.7 nm. (g) Schematic of our MoS_2 FET with 50 nm atomic-layer-deposition-grown Al_2O_3 as the gate dielectric and Pt/TiN/p^{++}-Si as the back-gate. The channel length (L) and width (W) were defined to be 500 nm and 5 μm, respectively. (h) Transfer characteristics, i.e., source-to-drain current (I_{DS}) versus back-gate voltage (V_{BG}), measured at a source-to-drain voltage V_{DS} = 1 V for a representative MoS_2 FET at room temperature (T = 300 K). (i) Output characteristics, i.e., I_{DS} versus V_{DS}, measured using different V_{BG} values for the same representative FET.

area.[33] In particular, when a single defect dominates the device response, discrete steps can be observed in the measured source-to-drain currents resulting in a random telegraph signal (RTS).[34] Statistical analysis of RTS allows for the extraction of the capture and emission time constants, trap level, activation energy, and even the physical location of the defects,[35] offering insights into the microscopic properties of the defects.

Stampfer *et al.*[36] observed RTS from single defects in scaled FETs based on exfoliated multilayer MoS_2 with a 50 nm × 50 nm channel area. They found these defects are located either in the bulk SiO_2, which was used as the back gate dielectric, or at the SiO_2/MoS_2 interface, or on top of the channel arising from adsorbed water molecules and processing contaminants. Fang *et al.*[37,38] and Li *et al.*[39] were also able to observe RTS in exfoliated mono- and multilayer MoS_2 FETs despite a relatively large channel area (~10−100 μm^2), albeit at low temperatures (<100 K). Interestingly, to the best of our knowledge, there is no report of observation of RTS in large-area synthetic monolayer MoS_2 FETs, although previous works involving high-resolution transmission electron microscopy (TEM) and scanning tunneling microscopy (STM) have suggested sulfur monovacancies as the most abundant defect type in synthetic MoS_2.[40,41]

Here, we report the observation of RTS in metal−organic chemical vapor deposition (MOCVD)-grown monolayer MoS_2-based FETs at varying gate biases and temperatures. By modeling the bias- and temperature-dependence of the capture and emission time constants with a nonradiative

https://doi.org/10.1021/acsnano.2c12900
ACS Nano 2023, 17, 14449−14460

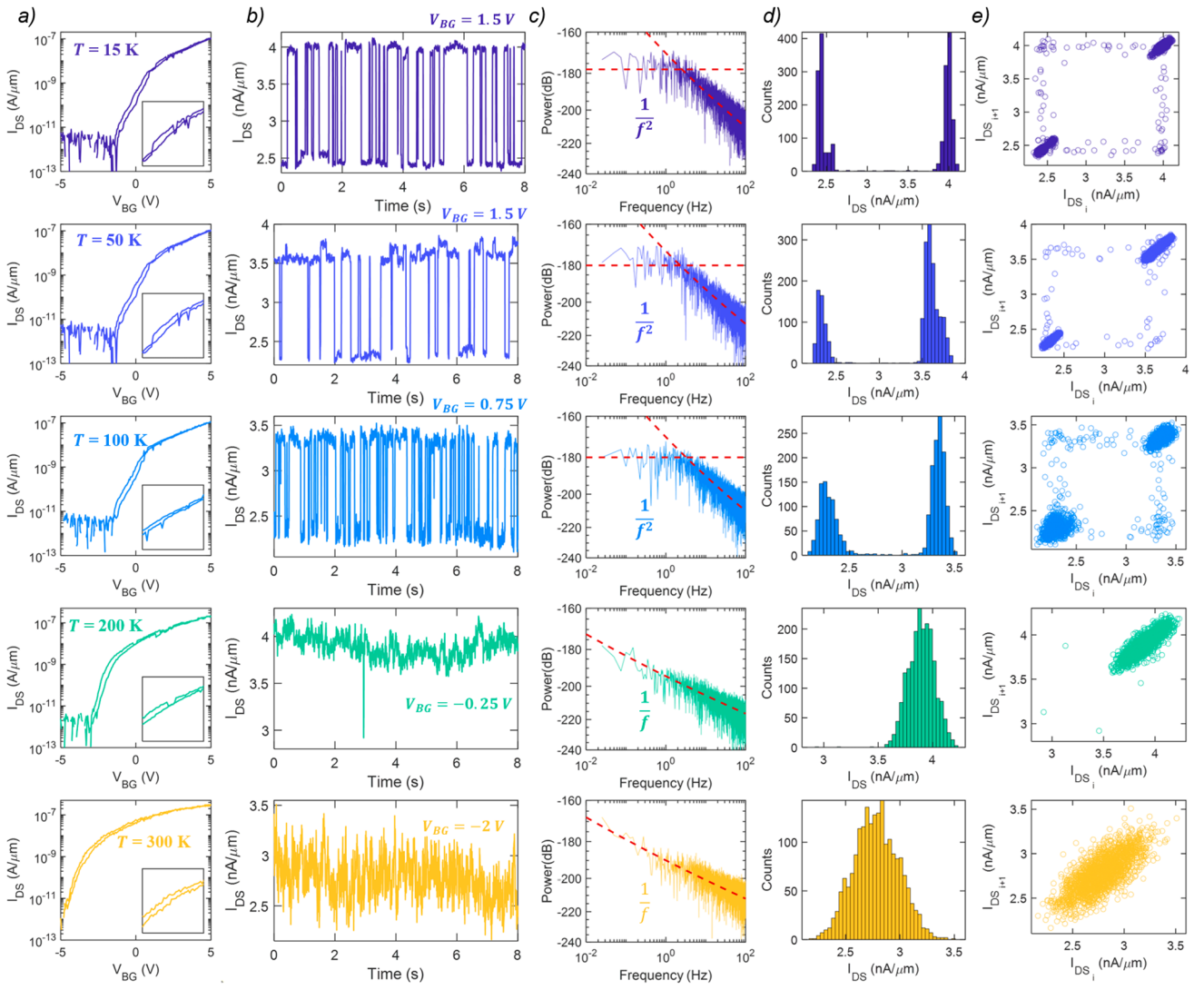

Figure 2. Observation of random telegraph signals (RTS) in a monolayer MoS_2 FET. (a) Transfer characteristics of a monolayer MoS_2 FET measured using V_{DS} = 1 V at different temperatures, T = 15, 50, 100, 200, and 300 K, and (b) corresponding I_{DS} sampled every τ_s = 4 ms at V_{BG} = 1.5, 1.5, 0.75, −0.25, and −2 V, respectively. RTS is observed for T < 200 K. (c) Power spectral density (PSD) obtained using the fast Fourier transform (FFT) of I_{DS} in (b). The presence of RTS is associated with a Lorentzian profile in the frequency domain, i.e., slope = $1/f^2$, whereas the absence of RTS is associated with a flicker noise profile in the frequency domain, i.e., slope = $1/f$. (d) Histogram plot for I_{DS} in (b). The presence of RTS is associated with two distinct Gaussian distributions, whereas the absence of RTS is associated with a single Gaussian distribution. (e) Time lag plot (TLP) for I_{DS} in (b). TLP involves the plotting of time-domain I_{DS} data in an x−y plane where the x-values represent the i^{th} time series data and the y-values represent the i+1th time series data for I_{DS}. In strictly two-level state transition dynamics corresponding to a single defect, one would expect a rectangular TLP with only the four corner points. However, at any finite temperature the discrete current points transform into clusters and the transition points get distributed along the arms of the rectangular feature. As the temperature increases, the clusters start to spread more and eventually coalesce into a single diagonal line, as seen from the TLPs corresponding to the I_{DS} measured at T > 200 K.

multiphonon model (NMP), possible defect candidates for the charge trapping in the Al_2O_3 gate oxide and their electronic and vibrational properties are identified. Several types of RTS are observed, including anomalous RTS and giant RTS indicating local current crowding effects and rich defect dynamics in synthetic monolayer MoS_2 FETs using Al_2O_3 as a gate dielectric.

Characterization of MOCVD-Grown Monolayer MoS_2 Films. The monolayer MoS_2 utilized for this study was grown using MOCVD on 1 cm^2 c-plane sapphire substrates at a temperature of 1000 °C. To ascertain the quality of the MoS_2 film used in this study, material characterization was performed using Raman spectroscopy and atomic force microscopy (AFM). Figure 1a shows the Raman spectra obtained from a representative MoS_2 film where the characteristic in-plane E^1_{2g} mode and out-of-plane A_{1g} mode were observed at 384 and 402 cm^{-1}, respectively, with a peak-to-peak distance of ∼18 cm^{-1}. Figure 1b,c show the Raman maps for E^1_{2g} and A_{1g} peak positions measured over a 50 μm × 50 μm area, respectively. The mean and standard deviation values for E^1_{2g} and A_{1g} were found to be ∼383.7 and ∼0.17 cm^{-1} and ∼401.8 and 0.14 cm^{-1}, respectively. Supplementary Figure 1 shows Raman maps for the peak separation and peak ratio between E^1_{2g} and A_{1g}, measured over a 50 μm × 50 μm area. Figure 1d shows the

https://doi.org/10.1021/acsnano.2c12900
ACS Nano 2023, 17, 14449−14460

photoluminescence (PL) spectra with a characteristic monolayer peak at 1.82 eV. Figure 1e shows the color map for the PL peak position, measured over a 50 μm × 50 μm area. The mean PL peak position was found to be at ∼1.83 eV with a standard deviation of ∼0.001 eV. The surface morphology and thickness of the film were characterized by AFM. Figure 1f shows the AFM micrograph of the MoS_2 film, indicating a coalesced monolayer film with a few oriented bilayer domains on top and a thickness of ∼0.7 nm. The underlying morphology in the monolayer region arises from the steps in the sapphire substrate. Nevertheless, the results of the material characterization indicate high-quality growth of the films.

Fabrication and Characterization of Monolayer MoS_2 FETs. The monolayer MoS_2 FETs employed for this study use a global back-gated architecture with 50 nm atomic-layer-deposition-grown Al_2O_3 as the gate dielectric and Pt/TiN/p^{++}-Si as the back-gate electrode. Figure 1g shows the schematic for the MoS_2 FET. The monolayer MoS_2 films were transferred from the growth substrates (sapphire) onto the target substrates via a poly(methyl methacrylate) (PMMA)-assisted wet-transfer process. Following the transfer, electron beam (e-beam) lithography and dry etching using SF_6 plasma were used to isolate the channel area. The channel length (L) and width (W) were defined to be 500 nm and 5 μm, respectively. Next, the source and drain contacts were defined using another set of e-beam exposures. Finally, e-beam evaporation was performed to sequentially deposit 40 nm of Ni and 30 nm of Au to serve as the contacts for the FETs. Details on monolayer MoS_2 synthesis, film transfer, and fabrication of the back-gate electrode stack and MoS_2 FETs can be found in the Methods section as well as in our recent works.[8−16,42] Figure 1h shows the transfer characteristics, i.e., source-to-drain current (I_{DS}) versus back-gate voltage (V_{BG}), measured at a source-to-drain voltage V_{DS} = 1 V for a representative MoS_2 FET at room temperature (T = 300 K). As expected, monolayer MoS_2 FETs exhibit dominant n-type transport owing to the pinning of the metal Fermi level close to the conduction band. Figure 1i shows the output characteristics, i.e., I_{DS} versus V_{DS}, measured using different V_{BG} values for the same representative FET.

Observation of RTS in Monolayer MoS_2 FETs. The impact of individual defects on silicon-based FETs has been extensively studied.[43] It is well known that the capture and emission of charges by the defect sites lead to a shift in the threshold voltage (V_{TH}) of the device, which manifests as hysteresis in the FET transfer characteristics. The stochastic nature of charge carrier capture and emission can lead to temporal fluctuations in the source-to-drain current when measured at constant source-to-gate and source-to-drain biases. In fact, discrete steps can be observed in I_{DS} if only a handful of defects are present in the channel area and cause notable changes in the electrostatics of the device. Such an I_{DS} profile is referred to as RTS. This is generally the case in ultrascaled devices where a reduction in the channel area leads to the confinement of a few defects with each defect having a considerable impact on the device characteristics. RTS can also be observed in relatively large-area devices when they are measured at low temperatures. This can be attributed to the fact that only a few defect states are energetically accessible for the charge carriers at low temperatures and that the current flow can be locally constrained, thereby causing sizable step heights.

Figure 2a shows the dual-sweep transfer characteristics of a monolayer MoS_2 FET measured using V_{DS} = 1 V at different temperatures, T = 15, 50, 100, 200, and 300 K. While the transfer characteristics, measured at all temperatures, show hysteresis, discrete steps are observed only at low temperatures, i.e., T < 300 K, as highlighted in the insets of Figure 2a. Figure 2b shows the I_{DS} sampled every τ_s = 4 ms at V_{BG} = 1.5, 1.5, 0.75, −0.25, and −2 V for T = 15, 50, 100, 200, and 300 K, respectively. Clearly, strong RTS signals are observed for T < 200 K. Note that different V_{BG} biases were chosen for the RTS measurements to ensure a similarly large I_{DS} range, hence a comparison of the RTS close to V_{TH}. Supplementary Figure 2 shows the I_{DS} measured at different V_{BG} values at these temperatures. As expected, the RTS signal is most prevalent at 15 K, gradually disappears with increasing T, and completely vanishes for T = 300 K. The temperature dependence of RTS can also be explained by analyzing the frequency spectrum of the time-domain I_{DS} measurements. Figure 2c shows the power spectral density (PSD) obtained by using the fast Fourier transform (FFT) of I_{DS} in Figure 2b. Supplementary Figure 3 shows the PSD obtained for the I_{DS} traces shown in Figure 2 corresponding to different V_{BG} and temperatures. Note that the PSD shows a characteristic $1/f$ profile for $T \geq$ 200 K, whereas a Lorentzian profile (slope = $1/f^2$) is observed for T < 200 K. This can be explained using the McWhorter model,[44] which states that carrier capture and emission by defect states in the dielectric are elastic tunneling events, and each event is associated with a characteristic time constant that is related to the depth profile of the corresponding defect. These discrete tunneling events manifest as RTS in the time domain and a Lorentzian spectrum in the frequency domain. Furthermore, the summation of all RTS events, each with different characteristic time constants, is the origin of the universally observed $1/f$ noise spectra in the frequency domain (see Supplementary Figure 4). In other words, at low temperatures, i.e., for T < 200 K, only one or a few energetically active defect states are accessible for carrier capture and emission leading to discrete state fluctuations or RTS in the time domain and a Lorentzian spectrum in the frequency domain, whereas at higher temperatures more defect states are accessible, resulting in the superposition of several discrete state RTS that leads to continuous fluctuations in the time domain and $1/f$ spectra in the frequency domain. Note that the elastic tunneling model cannot explain either the difference in capture and emission time constants that are typically observed or the pronounced temperature dependence of the capture time. To explain the temperature dependence, Kirton and Uren realized that the model needs to account for the structural relaxations at the defect site by introducing a phenomenological Boltzmann factor.[45] Their model was further refined in the NMP model,[33,46,47] where the gate bias and temperature dependence of the time constants are correctly described based on phonon-mediated structural relaxations at the defect site.

Another way to visualize the presence of RTS is to plot the histograms of the measured I_{DS}, as shown in Figure 2d. The presence of RTS is associated with the observation of two or more Gaussian distributions, as seen from the histograms corresponding to I_{DS} measured at T = 15, 50, and 100 K, whereas the absence of RTS is associated with a single Gaussian distribution, as seen from the histograms corresponding to I_{DS} measured at T = 200 and 300 K. Also note that the histogram plots for RTS traces with only two discrete states corresponding to the involvement of a single defect should

https://doi.org/10.1021/acsnano.2c12900
ACS Nano 2023, 17, 14449−14460

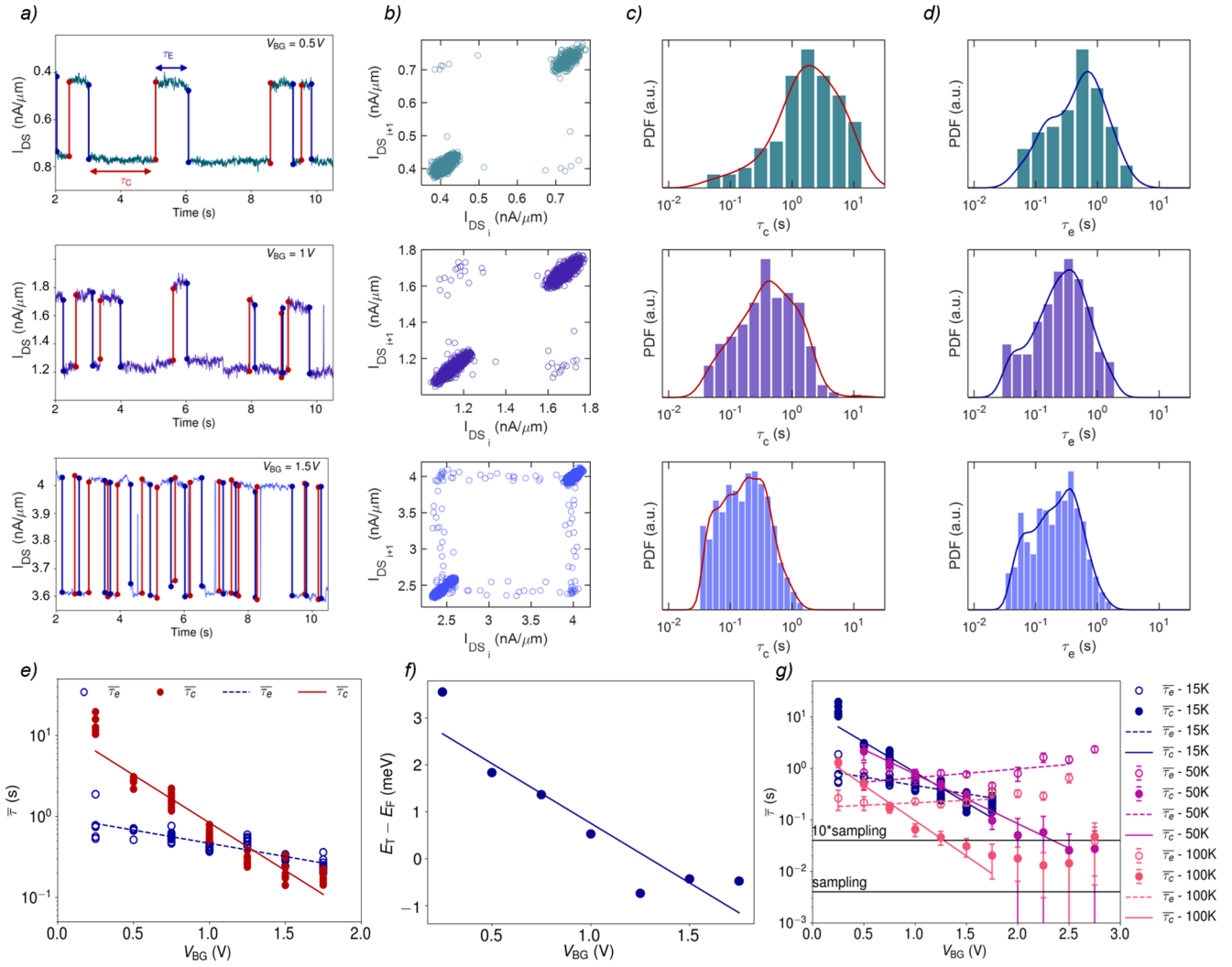

Figure 3. Gate-bias-dependent RTS for extracting energetic and physical locations of a defect. (a) RTS traces and (b) corresponding TLPs obtained for V_{BG} = 0.5, 1, and 1.5 V at T = 15 K. The V_{BG} range was chosen such that the two-state defect dynamics dominate. Here, the time spent in the lower state is referred to as the capture time, and the time spent in the upper state as the emission time, i.e., τ_c and τ_e, respectively. Normalized histogram plots on a logarithmic time scale for (c) τ_c and (d) τ_e showing the probability density of observing an event with a certain time constant. Insets show the Gaussian kernel density estimates used for extracting $\overline{\tau_c}$ and $\overline{\tau_e}$. (e) $\overline{\tau_e}$ and $\overline{\tau_c}$ as a function of V_{BG}. (f) The relative energetic location of the defect with respect to the Fermi level in the semiconducting channel, i.e., E_T−E_F as a function of V_{BG}. (g) $\overline{\tau_e}$ and $\overline{\tau_c}$ as a function of V_{BG} at temperatures of 15, 50, and 100 K.

translate into two delta distributions centered at the two current values. However, at a finite temperature, such distributions are always broadened into Gaussian distributions. With increasing temperature, the involvement of an increased number of defect states leads to broadening of the Gaussian distributions and introduction of additional distributions. Finally, at higher temperatures, e.g., for T > 200 K, the analog and random fluctuations in I_{DS} convert the histogram plots into one unified Gaussian distribution. While the PSD and histogram plots are useful techniques, these are less effective in reducing the complexity of the RTS waveform, which is a major obstacle in understanding the defect dynamics in nanoscale devices.

To overcome the aforementioned challenge, Nagumo *et al.*[48] have outlined the use of a time lag plot (TLP). A TLP involves the plotting of time-domain I_{DS} data in an x−y plane, where the x-values represent the i^{th} and the y-values represent the $i+1^{th}$ time series data for I_{DS}. Figure 2e shows the TLP corresponding to the I_{DS} shown in Figure 2b. Supplementary Figure 5 shows the TLPs obtained for the I_{DS} traces shown in Figure 2. In a TLP, the points along the diagonal represent different current values, whereas the points outside the diagonals represent state transitions. When RTS is present, multiple discrete clusters appear, as seen in the TLP corresponding to the I_{DS} measured at T < 200 K. In strictly two-level state transition dynamics corresponding to a single defect, one would expect a rectangular TLP with only the four corner points. However, at any finite temperature the discrete current points transform into clusters and the transition points get distributed along the sides of the rectangular frame. As the temperature increases, the clusters start to spread more and eventually coalesce into a single diagonal line, as seen from the TLPs corresponding to the I_{DS} measured at T > 200 K. Furthermore, TLPs also offer insight into how long the system spends on one of the two states as well as how often state transitions take place. In other words, they provide a visual

https://doi.org/10.1021/acsnano.2c12900
ACS Nano 2023, 17, 14449−14460

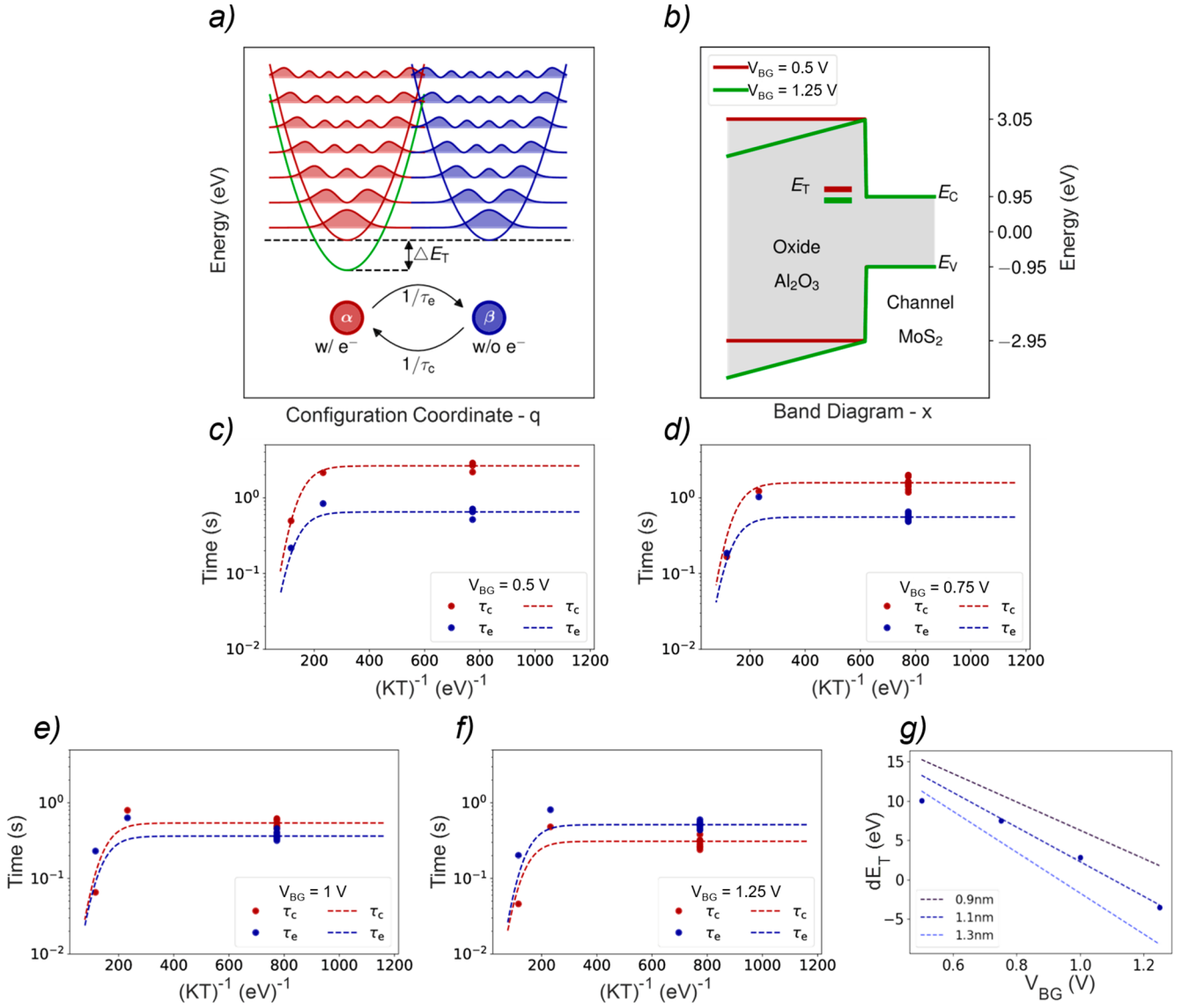

Figure 4. Modeling the temperature and gate-bias dependence to extract vibronic defect properties. (a) Configuration coordinate diagram for the transition of the defect configuration between the charged and the uncharged states. (b) Band diagram for Al_2O_3 and MoS_2 showing the energetic alignment of the trap level E_T, which is shifted by the applied gate bias at a gate contact to the left of the diagram. Modeled time constants as a function of temperature for different gate biases of (c) V_{BG} = 0.5 V, (d) 0.75 V, (e) 1 V, and (f) 1.25 V. For a relaxation energy of E_{relax} = 0.31 eV and a configuration coordinate distance of $\Delta Q = 2.03$ Å$\sqrt{u}$, the root-mean-square error amounts to 0.15 s. (g) The shift E_T of the charged state α as a function of the gate bias corresponds to a distance of 1.1 nm for the charge trap from the interface.

representation of the carrier capture and emission by the defect states.

A central drawback of the histogram and TLP methods is their reliance on absolute values of the signal for obtaining defect states. For example, a small drift of the drain current level over time can easily obfuscate defect states with smaller step heights, reducing the overall number of detected defects. Furthermore, both methods require a relatively high signal-to-noise ratio to work.[49] To overcome these difficulties, edge detection algorithms can be used to obtain the positions and amplitudes of the discrete steps in the RTS. In this work, we use the Canny edge detection algorithm to detect step edges based on a Gaussian derivative as a filter function.[50]

Gate-Bias-Dependent RTS for Extracting the Physical Location of Defects. Further insights into the defect dynamics can be obtained by studying the effect of V_{BG} on the RTS. Figure 3a shows the RTS traces obtained for V_{BG} = 0.5, 1, and 1.5 V at T = 15 K, and Figure 3b shows the corresponding TLPs. While the TLPs mostly exhibit two major clusters along the diagonals, for some V_{BG} values a metastable state is observed in the TLPs. However, for ease of analysis, we will ignore these metastable states and consider the dynamics to be primarily dominated by two states. This will allow us to extract the average capture and emission time constants, i.e., $\overline{\tau_c}$ and $\overline{\tau_e}$, which in turn will offer insights into the energetic location of the defect state. The two states in the TLP are denoted by clusters representing the lower and higher current values and the time spent in these two states is referred to as the capture and emission time, i.e., τ_c and τ_e, respectively. These times are evaluated as the difference between two subsequent step edges, detected with the Canny algorithm, as shown in Figure 3a; their respective distributions are shown in

https://doi.org/10.1021/acsnano.2c12900
ACS Nano 2023, 17, 14449−14460

Figure 3c,d as probability density functions (PDFs) of the exponentially distributed τ_c and τ_e on a logarithmic scale. Based on the Gaussian fits to the PDFs, $\overline{\tau_c}$ and $\overline{\tau_e}$ can be extracted. Figure 3e shows $\overline{\tau_c}$ and $\overline{\tau_e}$ as a function of V_{BG}. It is known that the ratio of $\overline{\tau_c}$ and $\overline{\tau_e}$ reflects the energetic location of the defect states with respect to the Fermi level (E_F) in the semiconducting channel following eq 1

$$\frac{\overline{\tau_c}}{\overline{\tau_e}} = \exp\left(\frac{E_T - E_F}{kT}\right) \tag{1}$$

where E_T is the energy level of the trap and k is the Boltzmann constant. Figure 3f shows $E_T - E_F$ as a function of V_{BG}. Note that, with increasing V_{BG}, τ_e is mostly constant while τ_c decreases. This implies that at a lower V_{BG}, e.g., at 0.5 V, the defect state is mostly empty for $\tau_c > \tau_e$, whereas at higher V_{BG}, e.g., at 2 V, the defect state is mostly occupied as the emission time is longer than the capture time ($\tau_e > \tau_c$). Finally, from the slope of Figure 3f, we can determine the physical location (λ) of the defect with respect to the thickness of the oxide (t_{ox}) using eq 2.

$$\frac{\lambda}{t_{ox}} = -\frac{kT}{q}\frac{\partial \ln\left(\overline{\tau_c}/\overline{\tau_e}\right)}{\partial V_{BG}} \tag{2}$$

We found that λ is ∼1.2 nm from the interface.

As a next step, we have applied the Canny algorithm and the formalism to extract the capture and emission time constants as described above to analyze the time constants as a function of the gate bias and the temperature, as shown in Figure 3g. During the analysis, we found that for increasing temperatures, e.g., 100 K and above, the time constants of the observed defect become increasingly fast, faster than the sampling time of τ_s = 4 ms. For extracting time constants to a high degree of certainty, they must be slower than about 10 times the sampling time, as shown in Figure 3g.

Modeling RTS for Extracting the Vibronic Defect Properties. To learn more about the atomic nature of the defect, we model the temperature and bias dependence of the capture and emission time constants using the NMP model.[46,47] When an electron is exchanged between a charge reservoir, such as the conduction band of MoS_2, and a local point defect in the vicinity, this charge transfer is accompanied by local deformations and relaxations of the defect sites. Hence, to accurately model RTS, electron−phonon coupling must be described with consideration for the movement of both electrons and nuclei. The atomic movements are represented within diabatic potential energy curves (i.e., crossing potential energy surfaces at a fixed charge state) along the reaction path of the charge transfer reaction. Such a configuration coordinate diagram for an oxide defect is shown in Figure 4a. The transition takes place between state α, where the defect has captured an electron, and state β, where there is no electron at the defect site. Both equilibrium states of the defect are approximated using a parabola. If a potential is applied to the gate, the potential shift of the parabola describing state α is given by the potential shift of the trap level within the oxide, as shown in Figure 4b and described by eq 3

$$\frac{dE_T}{dV_g} = \frac{q\lambda}{t_{ox}}\left(1 - \frac{d\psi_S}{dV_G}\right) \approx \frac{q\lambda}{t_{ox}} \tag{3}$$

with the surface potential ψ_S, an expression that is equivalent to eq 2 under the assumption of a constant surface potential in accumulation.

In the following, we evaluate this expression by modeling the temperature dependence of the capture and emission time constants for varying gate biases in a fully quantum mechanical NMP model. The background, assumptions, and derivation of this model are described in more detail in the Methods section. The NMP transition rates are the inverse of the experimentally determined capture and emission time constants ($k_C = 1/\tau_C = k_{ij}$) and are given by

$$\begin{aligned} k_{ij} &= A_{ij} f_{ij}^{LSF}, \\ f_{ij}^{LSF} &= \underset{\alpha}{ave}\left(\sum_\beta |\langle \eta_{i,\alpha}|\eta_{j,\beta}\rangle|^2\, \delta(E_{i,\alpha} - E_{j,\beta})\right), \\ A_{ij} &= \frac{2\pi}{\hbar}|\langle \Phi_i|H_{el}|\Phi_j\rangle|^2 \end{aligned} \tag{4}$$

with the electronic wave functions Φ_i, Φ_j, and the vibrational states $\eta_{i,\alpha}$, $\eta_{i,\beta}$, describing the nuclei configurations, the electronic matrix element A_{ij} determined by the electronic Hamiltonian H_{el}, and the line-shape function f_{ij}^{LSF} governing the vibrational interactions. A_{ij} can, in good approximation, be evaluated by the tunneling factor for the electron from the delocalized state at the band edge to the defect site within the Wentzel−Kramers−Brillouin (WKB) approximation. As such, A_{ij} is temperature independent. Hence, when studying the temperature dependence of the charge capture and emission processes, the line shape function needs to be evaluated. The vibrational wave functions of the two involved defect configurations can overlap not only at but also below the intersection point of the two parabolas, as shown in Figure 4a. These overlaps allow the system to transition at an effectively lower barrier, a phenomenon that is termed "nuclear tunneling".[47,51] To model the charge transfer rates at cryogenic temperatures, the line shape function as given in eq 4 is evaluated for the two harmonic defect states, as governed by the properties of the two parabolas in Figure 4a. First, they depend on the shift of the parabola of charged state E_T as a function of gate bias V_{BG}. Second, the cryogenic line shape function depends on the distance of the two parabolas and hence on the difference in the configuration coordinate ΔQ. Third, the transition rates depend on the shape of the parabolas, which is determined by the relaxation energy $E_{relax} = c_\alpha(\Delta Q)^2$, where c_α is the curvature of the parabola describing state α. The temperature dependence of the time constants in Figure 3g is modeled with three parameters, E_T, ΔQ, and E_{relax}. Out of these, E_T depends on the gate bias; hence, we can fit the temperature dependence for varying V_{BG} values with the same values for ΔQ and E_{relax} in Figure 4c−f with a small root mean squared error of 0.15 s. Another parameter set can be used to model the temperature dependence of the time constants to the same degree of accuracy, as shown in Supplementary Figure 6. Hence, these two parameter sets determine boundaries for the possible ranges of the parameter values. Based on the slope of the trap level shift E_T as a function of the applied gate voltage ΔV_{BG} shown in Figure 4g, according to eq 3, the interface distance can be estimated to be within the range of 1.1 and 1.2 nm. The trap level of the active defect was determined to be about 0.01 eV above the conduction band edge of MoS_2, which is about 3.9 eV above the valence band edge of Al_2O_3. All the vibrational and electronic properties of the observed defects causing RTS are summarized in Table 1.

https://doi.org/10.1021/acsnano.2c12900
ACS Nano 2023, 17, 14449−14460

Table 1. Defect Parameters of the Charge Trap Causing the RTS Signal[a]

defect parameter	lower limit	upper limit
relaxation energy E_{relax}	0.3 eV	1 eV
configuration coordinate distance ΔQ	2 Å$\sqrt{u}$	2.4 Å$\sqrt{u}$
trap level E_T above Al_2O_3 E_{VB}	3.9 eV	4 eV
interface distance d	1.1 nm	1.2 nm

[a]Parameters were extracted based on the modeled line shape function describing the low-temperature vibrational response of the charge transfer.

First, the distance of more than 1 nm from the interface shows that it is likely an oxide defect within the Al_2O_3 gate oxide which causes the observed RTS. The extracted defect level E_T is within a range that corresponds to the defect levels of an oxygen vacancy or an aluminum interstitial.[52] The vibronic properties, on the other hand (i.e., the small dQ), show that the charge transfer is dominated by nuclear tunneling, leading to the observed temperature independence at low temperatures. In non-glass-forming oxides like Al_2O_3 or HfO_2, the relaxation energies of point defects are typically on the order of about 1 eV,[52,53] further confirming the hypothesis of an oxygen vacancy or Al interstitial in the ALD-deposited Al_2O_3 causing the RTS.

Observation of Giant and Anomalous RTS. Giant RTS have been reported in the past for scaled Si FETs as well as carbon nanotube (CNT) FETs. Campbell *et al.*[54] have observed giant RTS in the subthreshold operation regime of a scaled n-type Si FET. Their RTS trace revealed $\frac{\Delta I_{DS}}{I_{DS}} > 25\%$, where ΔI_{DS} corresponds to the difference between the two discrete current levels. Similarly, Asenov *et al.*[55] have reported $\frac{\Delta I_{DS}}{I_{DS}}$ of ~60% in sub-100 nm Si FETs with dopant atoms. Fantini *et al.*[56] have investigated the RTS as a function of carrier concentration. Their study revealed that the measured RTS had an amplitude that was an order of magnitude higher than that predicted by the classical theory of carrier number and correlated mobility fluctuations. Beyond Si FETs, Liu *et al.*[57] observed giant RTS in ultrascaled CNT FETs with $\frac{\Delta I_{DS}}{I_{DS}}$ as high as 60%. Figure 5a shows the giant RTS obtained from our relatively large-area monolayer MoS_2 FETs measured at $T = 15$ K at a $V_{BG} = 1.5$ V. The $\frac{\Delta I_{DS}}{I_{DS}}$ was found to be ~80%. Figure 5b shows the corresponding TLP indicating the two discrete current levels. Figure 5c shows $\frac{\Delta I_{DS}}{I_{DS}}$ as a function of V_{BG}. Clearly, the RTS strength diminishes as the device is biased from the subthreshold into the on-state.

In general, it should be noted that the observation of an RTS signal in these large area devices is unusual, even more so in large step heights. For typical defect densities of 8×10^{11} cm^{-2} there should be as many as 20,000 defects within the device area of 2.5 μm^2. This approximate number is considerably above the single-defect limit of around 100 defects where one would expect to see charge capture and emission by single defects as RTS for specific bias and temperature conditions; see Figure 5d. The observation of single defect charge capture and emission is a strong indication that the channel is narrowed considerably at a certain point because of local defects, thereby reducing the effective active area of the MoS_2 FETs. In addition, the observed step heights of the RTS signals are much larger than what would be expected for devices with an area of 2.5 μm^2. In general, the step heights scale proportionally to the area of the FETs,[58] i.e., in a narrower and shorter channel, one defect has a larger impact on the electrostatics and the current flow. Hence, the observed large step heights must be explained by a defect located within the MoS_2 FET that is particularly critical for the current conduction. Based on these considerations, it seems plausible that the defect observed here is either an O vacancy or an Al interstitial close to the surface of the Al_2O_3 layer which is aligned close to a step edge of bilayer islands on top of the MOCVD-grown monolayer MoS_2 film, as the conduction of current across different layers is much smaller than within the layer. Moreover, potential contaminants at the interface of the wet-transferred, MOCVD-grown MoS_2 and the Al_2O_3 could also locally confine the current flow in the device. In addition,

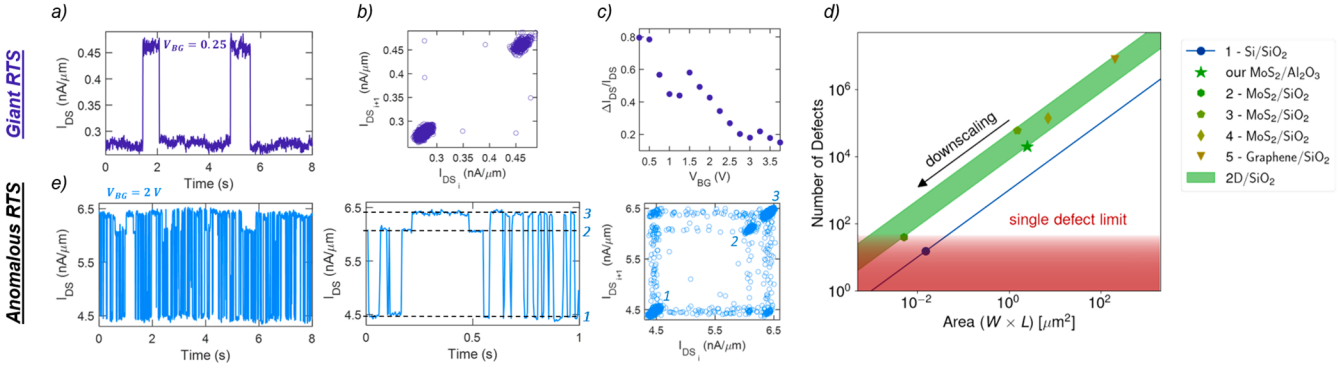

Figure 5. Rich defect dynamics in monolayer MoS_2 FET. (a) Giant RTS measured at $T = 15$ K at $V_{BG} = 1.5$ V. The $\frac{\Delta I_{DS}}{I_{DS}}$ was found to be ~80%. (b) Corresponding TLP indicating the two discrete current levels. (c) $\frac{\Delta I_{DS}}{I_{DS}}$ as a function of V_{BG}. RTS is expected if the number of defects within the device falls into the red-shaded area (i.e., the single defect limit), as shown in (d). For the MoS_2/Al_2O_3 FETs studied here, 20,000 active defects are expected to be located within the device area. As the single-defect limit is not reached, an effectively local narrowed channel region is observed. The border trap densities shown as symbols are taken from the literature: 1,[1] 2,[18] 3,[27] 4,[28] 5.[30] Anomalous RTS and corresponding TLPs showing (e) three discrete current levels. The RTS and the corresponding TLP in (e) indicate the involvement of a metastable state in addition to one regular trap state.

https://doi.org/10.1021/acsnano.2c12900
ACS Nano 2023, 17, 14449−14460

an oxide defect close to the source contact of the FET would cause larger step heights, as the charge injection over the Schottky barrier is a limiting factor in 2D-TMD-based FETs. All of the above factors could contribute to the effect of current crowding where the effective width of the FET is much narrower than the nominal 5 μm.

Apart from the normal two-state RTS induced by a single defect having two discrete current levels, a more complex RTS with multiple states has been observed in our monolayer MoS_2 FETs. These include RTS with three, four, and five discrete current levels. These types of RTS fall under the category of anomalous RTS with varying numbers of metastable states and have been reported in the literature.[59,60] Figure 5e shows the RTS traces and corresponding TLPs for three discrete current levels; Supplementary Figure 7 shows RTS traces for up to six current levels. Usually, a single trap state causes RTS with two current levels, whereas n trap states should lead to 2^n current levels in the RTS and 2^n clusters in the TLP. The involved states can be metastable and are linked to each other via either pure thermal transitions or charge transitions. In the first case, only a reconfiguration of the defect configuration takes place, whereas in the charge transition this is accompanied by an electron capture or emission event.[47,61] For example, the RTS and the corresponding TLP in Figure 5e indicate the involvement of a metastable state in addition to one regular trap state; hence, when the trap has captured an electron, it can either stabilize in the metastable state 2 or relax into state 3. These transitions are modeled within a hidden Markov model by connecting these three states in a Markov chain.[36,62] However, the more states that are involved, the more statistics that are required to extract the average capture and emission time constants as well as trap properties of all the involved states. In addition, more visible states in the signal render it increasingly difficult to distinguish between a defect with multiple states and two independent active charge traps that are superimposed in the signal; see also Supplementary Figure 7.

CONCLUSIONS

In conclusion, we have studied the dynamics of single defects in a large-area-grown monolayer MoS_2 FET. By changing the temperature and the gate bias, we can observe diverse RTS and extract information on the energetics, vibrational properties, and physical location of the defect. In this way, we observed nuclear tunneling at low temperatures and could identify charge trapping at an Al interstitial or O vacancy at about 1.2 nm distance from the interface as a dominant defect candidate. In addition, the observation of RTS signals and large step heights in these large-area 2D FETs indicates that oxide traps in the vicinity of the Schottky barriers at the contacts or close to step edges in the bilayer islands on top of MOCVD-grown monolayer MoS_2 could cause current crowding, thereby effectively narrowing the channel of the devices and increasing the step heights. Using detailed characterization and modeling techniques, we report the observation of RTS in FETs based on large-area-grown monolayer MoS_2 with ALD-grown Al_2O_3 as the gate dielectric. We also discuss various characterization approaches utilized in this study for RTS analysis including PSD, TLP, histogram plots, edge detection methods, and nonradiative multiphonon models. Finally, we discuss several types of RTS including giant RTS, multistate RTS, and anomalous RTS indicating rich defect dynamics in monolayer MoS_2 FETs.

METHODS

Large-Area Monolayer MoS_2 Film Growth. Uniform monolayer MoS_2 films are grown on 1 cm^2 c-plane sapphire substrates (Cryscore Optoelectronic Ltd., 99.996% purity) using a custom-built MOCVD system. The MOCVD chamber is equipped with a stainless-steel bubbler containing 10 g of $Mo(CO)_6$ (99.99% purity, Sigma-Aldrich), which serves as the Mo precursor source, and a 500 mL H_2S (99.5%, Sigma-Aldrich) lecture bottle, which provides sulfur during synthesis. Before introducing $Mo(CO)_6$ and H_2S, 2 slm of high-purity argon (Ar) gas is continuously flowed through the chamber and serves as the main push gas to deliver precursors to the substrate. During film synthesis, the chamber temperature and pressure are set to 1000 °C and 50 Torr, respectively. Like prior reports, we employ a multistep growth process comprising nucleation, ripening, and lateral growth stages to better control the nucleation rate on the sapphire substrates. $Mo(CO)_6$ is injected at flow rates of 1.5×10^{-3} and 7.5×10^{-4} sccm during the nucleation and lateral growth steps, respectively. H_2S flow is maintained at 20 sccm throughout the entire growth process. Complete monolayer coalescence is achieved after 42 min of total growth time.

H_2S Annealing. H_2S annealing is performed *ex situ* in the same MOCVD chamber used for MoS_2 film synthesis. Monolayer MoS_2 samples are placed on alumina crucibles (AdValue Tech, >99.6% purity) located at the center of the hot zone. The furnace is ramped up to 500 °C (the annealing temperature) at a rate of 50 °C/min; 40 sccm of H_2S and 2 slm are continuously flowed through the chamber and serve as the S source and push gas, respectively. The annealing process is carried out at a pressure of 50 Torr for a total time of 30 min.

Application Substrate Preparation and MoS_2 Film Transfer. To fabricate the 2D memtransistors, the MOCVD-grown monolayer MoS_2 film first had to be transferred from the sapphire growth substrate to the application substrate, which consisted of a global Al_2O_3/Pt/TiN/p^{++}-Si back-gate stack. The TiN and Pt layers were deposited using reactive sputtering onto the underlying Si to form a global back-gate electrode. A 50 nm layer of Al_2O_3 ($\varepsilon_{ox} \approx 10$) was grown on the Pt electrode via atomic layer deposition (ALD) to act as the back-gate dielectric. Film transfer was performed using a PMMA-assisted wet transfer process.[63,64] First, the as-grown MoS_2 on the sapphire substrate was spin-coated with PMMA and baked at 150 °C for 90 s to ensure good PMMA/MoS_2 adhesion. The edges of the spin-coated film were then scratched using a razor blade, and the substrate was immersed inside a deionized (DI) water bath held at 90 °C for 1 h. Capillary action caused the water to be preferentially drawn into the substrate/MoS_2 interface due to the hydrophilic nature of sapphire and the hydrophobic nature of MoS_2 and PMMA, separating the PMMA/MoS_2 stack from the sapphire substrate. The separated film was then fished from the water bath using the application substrate. Subsequently, the substrates were baked at 50 and 70 °C for 10 min each to remove moisture and promote film adhesion, thus ensuring pristine interfaces, before the PMMA was removed by immersing the samples in acetone for 12 h followed by a 30 min 2-propanol (IPA) cleaning.

Fabrication of 2D FETs. To define the channel regions of the MoS_2 FETs discussed in this work, the application substrates, with MoS_2 transferred on top, were spin-coated with PMMA A6 (4000 rpm for 45 s) and baked at 180 °C for 90 s. The resist was then exposed using electron beam (e-beam) lithography and developed using a 1:1 mixture of 4-methyl-2-pentanone (MIBK) and IPA(60 s) followed by pure IPA (45 s). The exposed monolayer MoS_2 film was subsequently etched using a sulfur hexafluoride (SF_6) reactive ion etch (RIE) recipe at 5 °C for 30 s. Next, the samples were rinsed in acetone and IPA to remove the e-beam resist. To define the source and drain contacts, samples were then spin-coated with a bilayer resist consisting of methyl methacrylate (MMA) and A3 PMMA. E-beam lithography was used to define the source and drain contacts, and development was performed using the same 1:1 mixture of MIBK and IPA. E-beam evaporation was used to deposit the contact metals (40/30 nm Ni/Au). Finally, a lift-off process was performed to remove

https://doi.org/10.1021/acsnano.2c12900
ACS Nano 2023, 17, 14449−14460

excess resist and metal by immersing the sample in acetone for 1 h followed by IPA for another 30 min.

Raman and Photoluminescence Spectroscopy. Raman and PL spectroscopy of the pre- and postirradiated MoS_2 film was performed using a Horiba LabRAM HR Evolution confocal Raman microscope with a 532 nm laser. The power was 34 mW filtered at 5% to 1.7 mW. The objective magnification was 100× with a numerical aperture of 0.9, and the grating had a spacing of 1800 gr/mm for Raman and 300 gr/mm for PL.

Electrical Characterization. Electrical characterization of the fabricated devices was performed in a Lake Shore CRX-VF probe station under atmospheric conditions using a Keysight B1500A parameter analyzer.

NMP Model. The nonradiative multiphonon model accounts for the electron−phonon coupling which drives the charge transfer between the atomic defect and the charge reservoir (i.e., conduction band) by modeling the reaction within diabatic potential energy curves in a parabolic approximation close to the minima of the potential energy curves. In a first-order perturbation approach, Fermi's golden rule can be applied to calculate the transition rate for the two states involved, consisting of both electrons, described by the electronic wave functions Φ_i, Φ_j, and nuclei states represented by the vibrational states $\eta_{i,\alpha}$, $\eta_{i,\beta}$,

$$k_{i\alpha,j\beta} = \frac{2\pi}{\hbar} |M_{i\alpha,j\beta}|^2 \, \delta(E_{i\alpha} - E_{j\beta}), \;\; |M_{i\alpha,j\beta}|^2 = \langle \eta_{i,\alpha} | \langle \Phi_i | H | \Phi_j \rangle | \eta_{j,\beta} \rangle \tag{2a}$$

Here, the Hamiltonian H describes the interaction between the electronic states and the vibrational states, and the transitions occur where the energies of the states of the initial state $E_{i\alpha}$ and the final state $E_{j\beta}$ are the same. As the electronic states vary only weakly with the nuclei coordinates, the Franck−Condon principle can be applied and the transition rate can be reformulated as a product of the electronic matrix element A_{ij} and the line shape function f_{ij}^{LSF}. While the matrix element describes the likelihood of an electronic transition, the line shape function contains all vibrational interactions caused by the lattice reconfigurations at the defect site. For describing these vibrational interactions, the sum over all modes β weighted by their respective occupation probabilities according to Boltzmann factors need to be formed and averaged over all populated initial states α. The NMP transition rates are the inverse of the experimentally determined capture and emission time constants ($k_C = 1/\tau_C = k_{ij}$) and are given by

$$k_{ij} = A_{ij} f_{ij}^{LSF}, \;\; f_{ij}^{LSF} = \underset{\alpha}{ave}\left(\sum_{\beta} |\langle \eta_{i,\alpha} | \eta_{j,\beta} \rangle|^2 \, \delta(E_{i,\alpha} - E_{j,\beta}) \right),$$
$$A_{ij} = \frac{2\pi}{\hbar} |\langle \Phi_i | H_{el} | \Phi_j \rangle|^2 \tag{4a}$$

with the electronic wave functions Φ_i, Φ_j and the vibrational states $\eta_{i,\alpha}$, $\eta_{i,\beta}$, describing the nuclei configurations. For more information about the evaluation of these expressions, see refs 46 and 47.

ASSOCIATED CONTENT

Data Availability Statement

The codes used for plotting and modeling the data are available from the corresponding authors on reasonable request.

Supporting Information

The Supporting Information is available free of charge at https://pubs.acs.org/doi/10.1021/acsnano.2c12900.

Supplementary figures (PDF)

AUTHOR INFORMATION

Corresponding Author

Saptarshi Das − *Engineering Science and Mechanics, Penn State University, University Park, Pennsylvania 16802, United States; Materials Science and Engineering, Materials Research Institute, and Electrical Engineering, Penn State University, University Park, Pennsylvania 16802, United States;* orcid.org/0000-0002-0188-945X; Email: sud70@psu.edu

Authors

Harikrishnan Ravichandran − *Engineering Science and Mechanics, Penn State University, University Park, Pennsylvania 16802, United States*

Theresia Knobloch − *Institute for Microelectronics (TU Wien), 1040 Vienna, Austria;* orcid.org/0000-0001-5156-9510

Andrew Pannone − *Engineering Science and Mechanics, Penn State University, University Park, Pennsylvania 16802, United States*

Alexander Karl − *Institute for Microelectronics (TU Wien), 1040 Vienna, Austria*

Bernhard Stampfer − *Institute for Microelectronics (TU Wien), 1040 Vienna, Austria;* orcid.org/0000-0001-5424-7488

Dominic Waldhoer − *Institute for Microelectronics (TU Wien), 1040 Vienna, Austria*

Yikai Zheng − *Engineering Science and Mechanics, Penn State University, University Park, Pennsylvania 16802, United States*

Najam U Sakib − *Engineering Science and Mechanics, Penn State University, University Park, Pennsylvania 16802, United States*

Muhtasim Ul Karim Sadaf − *Engineering Science and Mechanics, Penn State University, University Park, Pennsylvania 16802, United States*

Rahul Pendurthi − *Engineering Science and Mechanics, Penn State University, University Park, Pennsylvania 16802, United States*

Riccardo Torsi − *Materials Science and Engineering, Penn State University, University Park, Pennsylvania 16802, United States*

Joshua A. Robinson − *Materials Science and Engineering, Department of Chemistry, and Department of Physics, Penn State University, University Park, Pennsylvania 16802, United States*

Tibor Grasser − *Institute for Microelectronics (TU Wien), 1040 Vienna, Austria*

Complete contact information is available at: https://pubs.acs.org/10.1021/acsnano.2c12900

Author Contributions

H.R. and T.K. are equal contribution authors.

Notes

The authors declare no competing financial interest.

ACKNOWLEDGMENTS

The work of H.R., A.P., Y.Z., N.U.S., M.U.K.S., R.P., and S.D. was supported by the Army Research Office (ARO) through Contract Number W911NF1920338 and National Science Foundation (NSF) through a CAREER Award under grant no. ECCS-2042154. The authors also acknowledge the materials support from the National Science Foundation (NSF) through the Pennsylvania State University 2D Crystal Consortium−Materials Innovation Platform (2DCCMIP) under NSF cooperative agreement DMR-2039351. This work was also

supported by the Department of Defense, Defense Threat Reduction Agency (DTRA), as part of the Interaction of Ionizing Radiation with Matter University Research Alliance (IIRM-URA) under contract number HDTRA1-20-2-0002. The content of the information does not necessarily reflect the position or the policy of the federal government, and no official endorsement should be inferred. T.K., A.K., B.S., D.W., and T.G. acknowledge support from the European Research Council under Grant 101055379. R.T. and J.A.R. acknowledge funding from NEWLIMITS, a center in nCORE as part of the Semiconductor Research Corporation (SRC) program sponsored by NIST through award number 70NANB17H041, as well as NSF ECCS-2202280 and NSF DMR-2039351. H.R. would like to thank Sai Venkata Gayathri Ayyagari for her help with the preparation of the TOC.

REFERENCES

(1) Das, S.; et al. Transistors based on two-dimensional materials for future integrated circuits. *Nature Electronics* **2021**, *4* (11), 786−799.
(2) Akinwande, D.; et al. Graphene and two-dimensional materials for silicon technology. *Nature* **2019**, *573* (7775), 507−518.
(3) Chhowalla, M.; Jena, D.; Zhang, H. Two-dimensional semiconductors for transistors. *Nature Reviews Materials* **2016**, *1* (11), 1−15.
(4) Zhu, K.; et al. The development of integrated circuits based on two-dimensional materials. *Nature Electronics* **2021**, *4* (11), 775−785.
(5) Wachter, S.; Polyushkin, D. K.; Bethge, O.; Mueller, T. A microprocessor based on a two-dimensional semiconductor. *Nat. Commun.* **2017**, *8*, 14948.
(6) Gao, Q.; Zhang, Z.; Xu, X.; Song, J.; Li, X.; Wu, Y. Scalable high performance radio frequency electronics based on large domain bilayer MoS2. *Nat. Commun.* **2018**, *9* (1), 4778.
(7) Polyushkin, D. K.; et al. Analogue two-dimensional semiconductor electronics. *Nature Electronics* **2020**, *3* (8), 486−491.
(8) Zheng, Y.; Ravichandran, H.; Schranghamer, T. F.; Trainor, N.; Redwing, J. M.; Das, S. Hardware implementation of Bayesian network based on two-dimensional memtransistors. *Nat. Commun.* **2022**, *13* (1), 5578.
(9) Sebastian, A.; et al. Two-dimensional materials-based probabilistic synapses and reconfigurable neurons for measuring inference uncertainty using Bayesian neural networks. *Nat. Commun.* **2022**, *13* (1), 1−10.
(10) Sebastian, A.; Das, S.; Das, S. An Annealing Accelerator for Ising Spin Systems Based on In-Memory Complementary 2D FETs. *Adv. Mater.* **2022**, *34* (4), 2107076.
(11) Pendurthi, R.; et al. Heterogeneous Integration of Atomically Thin Semiconductors for Non-von Neumann CMOS. *Small* **2022**, *18*, 2202590.
(12) Dodda, A.; Trainor, N.; Redwing, J.; Das, S. All-in-one, bio-inspired, and low-power crypto engines for near-sensor security based on two-dimensional memtransistors. *Nat. Commun.* **2022**, *13* (1), 1−12.
(13) Chakrabarti, S.; et al. Logic Locking of Integrated Circuits Enabled by Nanoscale MoS2-Based Memtransistors. *ACS Applied Nano Materials* **2022**, *5*, 14447.
(14) Sebastian, A.; Pendurthi, R.; Choudhury, T. H.; Redwing, J. M.; Das, S. Benchmarking monolayer MoS2 and WS2 field-effect transistors. *Nat. Commun.* **2021**, *12* (1), 693.
(15) Oberoi, A.; Dodda, A.; Liu, H.; Terrones, M.; Das, S. Secure Electronics Enabled by Atomically Thin and Photosensitive Two-Dimensional Memtransistors. *ACS Nano* **2021**, *15* (12), 19815−19827.
(16) Jayachandran, D.; et al. A low-power biomimetic collision detector based on an in-memory molybdenum disulfide photodetector. *Nature Electronics* **2020**, *3* (10), 646−655.
(17) Geng, D.; Yang, H. Y. Recent advances in growth of novel 2D materials: beyond graphene and transition metal dichalcogenides. *Adv. Mater.* **2018**, *30* (45), 1800865.
(18) Schranghamer, T. F.; Sharma, M.; Singh, R.; Das, S. Review and comparison of layer transfer methods for two-dimensional materials for emerging applications. *Chemical Society Reviews* **2021**, *50*, 11032.
(19) Lanza, M.; Smets, Q.; Huyghebaert, C.; Li, L. J. Yield, variability, reliability, and stability of two-dimensional materials based solid-state electronic devices. *Nat. Commun.* **2020**, *11* (1), 5689.
(20) Shen, P.-C.; et al. Ultralow contact resistance between semimetal and monolayer semiconductors. *Nature* **2021**, *593* (7858), 211−217.
(21) Li, S.-L.; Tsukagoshi, K.; Orgiu, E.; Samorì, P. Charge transport and mobility engineering in two-dimensional transition metal chalcogenide semiconductors. *Chem. Soc. Rev.* **2016**, *45* (1), 118−151.
(22) Schulman, D. S.; Arnold, A. J.; Das, S. Contact engineering for 2D materials and devices. *Chem. Soc. Rev.* **2018**, *47*, 3037.
(23) Asselberghs, I.; et al., Scaled transistors with 2D materials from the 300mm fab. *2020 IEEE Silicon Nanoelectronics Workshop (SNW)* 2020; IEEE, pp 67−68, DOI: 10.1109/snw50361.2020.9131651.
(24) Smets, Q.; et al. Ultra-scaled MOCVD MoS 2 MOSFETs with 42nm contact pitch and 250μA/μm drain current. In *2019 IEEE International Electron Devices Meeting (IEDM)*; 2019: IEEE, pp 23.2.1−23.2.4.
(25) Degraeve, R.; et al. Trap spectroscopy by charge injection and sensing (TSCIS): A quantitative electrical technique for studying defects in dielectric stacks. In *2008 IEEE International Electron Devices Meeting*; IEEE, 2008; pp 1−4.
(26) Illarionov, Y. Y.; et al. Energetic mapping of oxide traps in MoS2 field-effect transistors. *2D Materials* **2017**, *4* (2), 025108.
(27) Illarionov, Y. Y.; et al. The role of charge trapping in MoS2/SiO2 and MoS2/hBN field-effect transistors. *2D Materials* **2016**, *3* (3), 035004.
(28) Schroder, D. K.; Babcock, J. A. Negative bias temperature instability: Road to cross in deep submicron silicon semiconductor manufacturing. *J. Appl. Phys.* **2003**, *94* (1), 1−18.
(29) Guo, Y.; et al. Charge trapping at the MoS2-SiO2 interface and its effects on the characteristics of MoS2 metal-oxide-semiconductor field effect transistors. *Appl. Phys. Lett.* **2015**, *106* (10), 103109.
(30) Park, Y.; Baac, H. W.; Heo, J.; Yoo, G. Thermally activated trap charges responsible for hysteresis in multilayer MoS2 field-effect transistors. *Appl. Phys. Lett.* **2016**, *108* (8), 083102.
(31) Late, D. J.; Liu, B.; Matte, H. S. S. R.; Dravid, V. P.; Rao, C. N. R. Hysteresis in single-layer MoS2 field effect transistors. *ACS Nano* **2012**, *6* (6), 5635−41.
(32) Arnold, A. J.; Razavieh, A.; Nasr, J. R.; Schulman, D. S.; Eichfeld, C. M.; Das, S. Mimicking Neurotransmitter Release in Chemical Synapses via Hysteresis Engineering in MoS2 Transistors. *ACS Nano* **2017**, *11* (3), 3110−3118.
(33) Grasser, T. Stochastic charge trapping in oxides: From random telegraph noise to bias temperature instabilities. *Microelectronics Reliability* **2012**, *52* (1), 39−70.
(34) Yuzhelevski, Y.; Yuzhelevski, M.; Jung, G. Random telegraph noise analysis in time domain. *Rev. Sci. Instrum.* **2000**, *71* (4), 1681−1688.
(35) Grill, A.; et al.Characterization and modeling of single defects in GaN/AlGaN fin-MIS-HEMTs. In *2017 IEEE International Reliability Physics Symposium (IRPS)*; IEEE, 2017; pp 3B-5.1−3B-5.5.
(36) Stampfer, B.; et al. Characterization of Single Defects in Ultrascaled MoS_2 Field-Effect Transistors. *ACS Nano* **2018**, *12* (6), 5368−5375.
(37) Nan, F.; Nagashio, K.; Toriumi, A. Subthreshold transport in mono-and multilayered MoS2 FETs. *Appl. Phys. Express* **2015**, *8* (6), 065203.
(38) Fang, N.; Nagashio, K.; Toriumi, A. Experimental detection of active defects in few layers MoS2 through random telegraphic signals analysis observed in its FET characteristics. *2D Materials* **2017**, *4* (1), 015035.

(39) Li, L.; Lee, I.; Youn, D.-H.; Kim, G.-H. Hopping conduction and random telegraph signal in an exfoliated multilayer MoS2 field-effect transistor. *Nanotechnology* **2017**, *28* (7), 075201.
(40) Hong, J.; et al. Exploring atomic defects in molybdenum disulphide monolayers. *Nat. Commun.* **2015**, *6* (1), 1−8.
(41) Zhou, W.; et al. Intrinsic structural defects in monolayer molybdenum disulfide. *Nano Lett.* **2013**, *13* (6), 2615−2622.
(42) Ravichandran, H.; Zheng, Y.; Schranghamer, T. F.; Trainor, N.; Redwing, J. M.; Das, S. A Monolithic Stochastic Computing Architecture for Energy Efficient Arithmetic. *Adv. Mater.* **2023**, *35* (2), 2206168.
(43) Grasser, T.; et al. Gate-sided hydrogen release as the origin of "permanent" NBTI degradation: From single defects to lifetimes. In *2015 IEEE International Electron Devices Meeting (IEDM)*, 7−9 Dec. 2015; IEEE, 2015; pp 20.1.1−20.1.4, DOI: 10.1109/IEDM.2015.7409739.
(44) McWhorter, A. L. 1/f noise and related surface effects in germanium. Sc.D. thesis, 1955.
(45) Kirton, M. J.; Uren, M. J. Noise in solid-state microstructures: A new perspective on individual defects, interface states and low-frequency (1/*f*) noise. *Adv. Phys.* **1989**, *38* (4), 367−468.
(46) Alkauskas, A.; Yan, Q.; Van de Walle, C. G. First-principles theory of nonradiative carrier capture via multiphonon emission. *Phys. Rev. B* **2014**, *90* (7), 075202.
(47) Goes, W.; et al. Identification of oxide defects in semiconductor devices: A systematic approach linking DFT to rate equations and experimental evidence. *Microelectronics Reliability* **2018**, *87*, 286−320.
(48) Nagumo, T.; Takeuchi, K.; Yokogawa, S.; Imai, K.; Hayashi, Y. New analysis methods for comprehensive understanding of Random Telegraph Noise. In *2009 IEEE International Electron Devices Meeting (IEDM)*, 7−9 Dec. 2009; IEEE, 2009; pp 1−4, DOI: 10.1109/IEDM.2009.5424230.
(49) Martin-Martinez, J.; Diaz, J.; Rodriguez, R.; Nafria, M.; Aymerich, X. New Weighted Time Lag Method for the Analysis of Random Telegraph Signals. *IEEE Electron Device Lett.* **2014**, *35* (4), 479−481.
(50) Canny, J. A Computational Approach to Edge Detection. In *IEEE Transactions on Pattern Analysis and Machine Intelligence*; IEEE, 1986; Vol. PAMI-*8*, no. 6, pp 679−698, DOI: 10.1109/TPAMI.1986.4767851.
(51) Michl, J.; et al. Evidence of Tunneling Driven Random Telegraph Noise in Cryo-CMOS. In *2021 IEEE International Electron Devices Meeting (IEDM)*, 11−16 Dec. 2021; IEEE, 2021; pp 31.3.1−31.3.4, DOI: 10.1109/IEDM19574.2021.9720501.
(52) Dicks, O. A.; Cottom, J.; Shluger, A. L.; Afanas'ev, V. V. The origin of negative charging in amorphous Al2O3 films: the role of native defects. *Nanotechnology* **2019**, *30* (20), 205201.
(53) Strand, J.; La Torraca, P.; Padovani, A.; Larcher, L.; Shluger, A. L. Dielectric breakdown in HfO2 dielectrics: Using multiscale modeling to identify the critical physical processes involved in oxide degradation. *J. Appl. Phys.* **2022**, *131* (23), 234501.
(54) Campbell, J. P.; et al. Large random telegraph noise in sub-threshold operation of nano-scale nMOSFETs. In *2009 IEEE International Conference on IC Design and Technology*, 18−20 May 2009; IEEE, 2009; pp 17−20, DOI: 10.1109/ICICDT.2009.5166255.
(55) Asenov, A.; Balasubramaniam, R.; Brown, A. R.; Davies, J. H.; Saini, S. Random telegraph signal amplitudes in sub 100 nm (decanano) MOSFETs: a 3D 'Atomistic' simulation study. In *International Electron Devices Meeting 2000*; 10−13 Dec. 2000; 2000; IEDM, pp 279−282, DOI: 10.1109/IEDM.2000.904311.
(56) Fantini, P.; Ghetti, A.; Marinoni, A.; Ghidini, G.; Visconti, A.; Marmiroli, A. Giant Random Telegraph Signals in Nanoscale Floating-Gate Devices. *IEEE Electron Device Lett.* **2007**, *28* (12), 1114−1116.
(57) Liu, F.; et al. Giant random telegraph signals in the carbon nanotubes as a single defect probe. *Appl. Phys. Lett.* **2005**, *86* (16), 163102.
(58) Asenov, A.; Balasubramaniam, R.; Brown, A. R.; Davies, J. H. RTS amplitudes in decananometer MOSFETs: 3-D simulation study. *IEEE Trans. Electron Devices* **2003**, *50* (3), 839−845.
(59) Wang, R.; Guo, S.; Zhang, Z.; Zou, J.; Mao, D.; Huang, R. Complex Random Telegraph Noise (RTN): What Do We Understand? In *2018 IEEE International Symposium on the Physical and Failure Analysis of Integrated Circuits (IPFA)*, 16−19 July 2018; IEEE, 2018; pp 1−7, DOI: 10.1109/IPFA.2018.8452514.
(60) Uren, M. J.; Kirton, M. J.; Collins, S. Anomalous telegraph noise in small-area silicon metal-oxide-semiconductor field-effect transistors. *Phys. Rev. B* **1988**, *37* (14), 8346−8350.
(61) Wilhelmer, C.; et al. Ab initio investigations in amorphous silicon dioxide: Proposing a multi-state defect model for electron and hole capture. *Microelectronics Reliability* **2022**, *139*, 114801.
(62) Puglisi, F. M.; Pavan, P.; Padovani, A.; Larcher, L.; Bersuker, G. RTS noise characterization of HfOx RRAM in high resistive state. *Solid-State Electron.* **2013**, *84*, 160−166.
(63) Zhang, F.; Erb, C.; Runkle, L.; Zhang, X.; Alem, N. Etchant-free transfer of 2D nanostructures. *Nanotechnology* **2018**, *29* (2).
(64) Sebastian, A.; et al. Electrochemical Polishing of Two-Dimensional Materials. *ACS Nano* **2019**, *13* (1), 78−86.

https://doi.org/10.1021/acsnano.2c12900
ACS Nano 2023, 17, 14449−14460